Available online at www.sciencedirect.com
SCIENCE DIRECT®
Journal of Computational Physics 190 (2003) 141–158
JOURNAL OF COMPUTATIONAL PHYSICS
www.elsevier.com/locate/jcp

# Numerical methods for semiconductor heterostructures with band nonparabolicity

Weichung Wang [a,*], Tsung-Min Hwang [b], Wen-Wei Lin [c], Jinn-Liang Liu [d]

[a] Department of Applied Mathematics, National University of Kaohsiung, Kaohsiung 811, Taiwan
[b] Department of Mathematics, National Taiwan Normal University, Taipei 116, Taiwan
[c] Department of Mathematics, National Tsing Hua University, Hsinchu 300, Taiwan
[d] Department of Applied Mathematics, National Chiao Tung University, Hsinchu 300, Taiwan

Received 12 November 2002; received in revised form 8 May 2003; accepted 13 May 2003

**Abstract**

This article presents numerical methods for computing bound state energies and associated wave functions of three-dimensional semiconductor heterostructures with special interest in the numerical treatment of the effect of band nonparabolicity. A nonuniform finite difference method is presented to approximate a model of a cylindrical-shaped semiconductor quantum dot embedded in another semiconductor matrix. A matrix reduction method is then proposed to dramatically reduce huge eigenvalue systems to relatively very small subsystems. Moreover, the nonparabolic band structure results in a cubic type of nonlinear eigenvalue problems for which a cubic Jacobi–Davidson method with an explicit nonequivalence deflation method are proposed to compute all the desired eigenpairs. Numerical results are given to illustrate the spectrum of energy levels and the corresponding wave functions in rather detail.


*Keywords:* Semiconductor quantum dot; The Schrödinger equation; Energy levels; Wave functions; Cubic eigenvalue problems; Matrix reduction; Cubic Jacobi–Davidson method; Explicit nonequivalence deflation

## 1. Introduction

Nanoscale semiconductor quantum dots (QDs) have been intensively studied in their physics [1–3] and applications [4–8]. In addition to theoretical and experimental methods, numerical simulations can also provide useful insights into a QDs electronic and optical properties [9–11]. However, effective and feasible numerical methods for three-dimensional (3D) quantum structures are rarely available [12, Section 11.6].

This article presents some novel methods for calculating bound state energies and their corresponding wave functions of a 3D QD model for which the numerical treatment of band nonparabolicity is of special interest.

* Corresponding author. Tel.: +886-7-591-9521; fax: +886-7-591-9344.
*E-mail addresses:* wwang@nuk.edu.tw (W. Wang), min@math.ntnu.edu.tw (T.-M. Hwang), wwlin@am.nthu.edu.tw (W.-W. Lin), jinnliu@math.nctu.edu.tw (J.-L. Liu).

0021-9991/$ - see front matter 
doi:10.1016/S0021-9991(03)00268-7

The model assumes a single cylindrical low-bandgap semiconductor island embedded in a wide-bandgap semiconductor matrix, one-band envelope-function approximation, BenDaniel–Duke boundary conditions, and nonparabolic band structure. This model is proposed in [13] and later used and extended in various works [14–16] and in references therein. This is a model that accounts for the effect of spin–orbit splitting in semiconductor heterostructures. One of the major applications of the spin–orbit splitting effect in quantum electronic devices is to develop a new branch of semiconductor electronics, so-called spintronics [17–20].

The Schrödinger equation of the model is discretized by finite difference approximation in cylindrical coordinates with nonuniform mesh by which more grid points are placed around the heterojunction. In order to retain comparable accuracy of numerical energies with that of experimental values of momentum, energy gap, and spin–orbit splitting etc., the matrix size of the resulting eigenvalue problems can be up to as much as 98 millions for some typical size of QD. Our first method is a matrix reduction scheme which consists of three steps: block diagonalizing the coefficient matrix, reordering the unknown eigenvector, and transforming into a block diagonal system. As a result, the original system is then transformed to a set of, for instance, seven subsystems with the matrix size of 274 thousands. The reduction dramatically reduce the computational time and storage.

The second difficulty for the numerical treatment of the model is caused by band nonparabolicity which results in a cubic type of eigenvalue systems. To our knowledge, effective methods for solving cubic eigenvalue problems such as that presented here are not available in the literature. A cubic version of the Jacobi–Davidson method is proposed to tackle this difficulty. Moreover, since we are interested in obtaining all possible bound states of the model, a new deflation scheme is also presented to successively compute energies from the ground state up to all excited states. Numerical results are given to demonstrate the efficiency and accuracy of the proposed methods.

This article is organized as follows. The model is stated in Section 2. The finite difference approximation of the model and the matrix reduction method are given in Section 3. Section 4 presents the cubic Jacobi–Davidson method and the explicit nonequivalence low-rank deflation method written in algorithmic format for a better illustration of the numerical procedures in implementation. Numerical results with 3D graphics of wave functions are given in Section 5. Some concluding remarks are made in Section 6.

## 2. The model problem

We consider a model of a cylindrical CdTe QD embedded in the center of a cylindrical InSb matrix as shown in Fig. 1 [16]. It is natural to use cylindrical coordinates, namely, the radial coordinate $r$, the

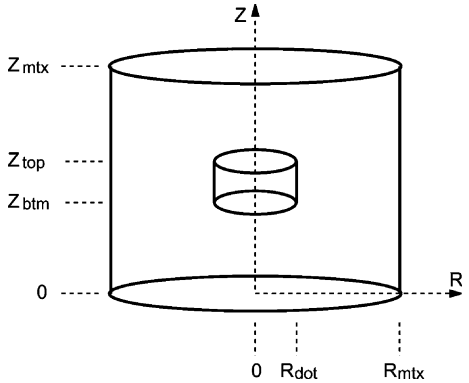


Fig. 1. Structure schema of a cylindrical quantum dot and the heterostructure matrix. $R_{\mathrm{dot}}$ and $R_{\mathrm{mtx}}$ denote the radii of the dot and the matrix, respectively. $Z_{\mathrm{btm}}$ and $Z_{\mathrm{top}}$ (0 and $Z_{\mathrm{mtx}}$) denote the bottom and top of the dot (matrix).

azimuthal angle $\theta$, and the natural axial coordinate $z$, to specify an arbitrary position within the target domain. More specifically, the $z$ coordinates of the bottom and top of the matrix (the dot) are 0 and $Z_{\mathrm{mtx}}$ ($Z_{\mathrm{btm}}$ and $Z_{\mathrm{top}}$), respectively, and the radii of the dot and the matrix are denoted by $R_{\mathrm{dot}}$ and $R_{\mathrm{mtx}}$, respectively.

The Schrödinger equation approximating the model is

$$\frac{-\hbar^2}{2m_\ell(\lambda)}\left[\frac{\partial^2 F}{\partial r^2}+\frac{1}{r}\frac{\partial F}{\partial r}+\frac{1}{r^2}\frac{\partial^2 F}{\partial \theta^2}+\frac{\partial^2 F}{\partial z^2}\right]+c_\ell F=\lambda F, \tag{1}$$

where $\hbar$ is the reduced Planck constant, $\lambda$ is the total electron energy, $F=F(r,\theta,z)$ is the wave function, $m_\ell(\lambda)$ and $c_\ell$ are the electron effective mass and confinement potential in the $\ell$th region. The index $\ell$ is used to distinguish the region of the QD (for $\ell=1$) from that of the matrix (for $\ell=2$). Since we expect significant effect of spin–orbit splitting in narrow gap semiconductors, it is important to take into account the nonparabolicity for the electron's dispersion relation for which the effective mass is given as [13]

$$\frac{1}{m_\ell(\lambda)}=\frac{P_\ell^2}{\hbar^2}\left(\frac{2}{\lambda+g_\ell-c_\ell}+\frac{1}{\lambda+g_\ell-c_\ell+\delta_\ell}\right), \tag{2}$$

where $P_\ell$, $g_\ell$, and $\delta_\ell$ are the momentum, main energy gap, and spin–orbit splitting in the $\ell$th region, respectively. In our numerical experiments, the values of these parameters are $c_1=0.000$, $g_1=0.235$, $\delta_1=0.81$, $P_1=0.2875$, $c_2=0.350$, $g_2=1.590$, $\delta_2=0.80$, and $P_2=0.1993$.

For Eq. (1), Dirichlet boundary conditions are prescribed on the top, bottom, and wall of the matrix, i.e.,

$$F(r,\theta,Z_{\mathrm{mtx}})=F(r,\theta,0)=F(R_{\mathrm{mtx}},\theta,z)=0. \tag{3}$$

Moreover, the following BenDaniel–Duke boundary conditions are imposed on the interface of the two different materials:

$$\begin{aligned}
\frac{\hbar^2}{2m_1(\lambda)}\frac{\partial F}{\partial r}\bigg|_{R_{\mathrm{dot}}^-} &= \frac{\hbar^2}{2m_2(\lambda)}\frac{\partial F}{\partial r}\bigg|_{R_{\mathrm{dot}}^+},\\
\frac{\hbar^2}{2m_1(\lambda)}\frac{\partial F}{\partial z}\bigg|_{Z_{\mathrm{btm}}^-} &= \frac{\hbar^2}{2m_2(\lambda)}\frac{\partial F}{\partial z}\bigg|_{Z_{\mathrm{btm}}^+},\\
\frac{\hbar^2}{2m_1(\lambda)}\frac{\partial F}{\partial z}\bigg|_{Z_{\mathrm{top}}^-} &= \frac{\hbar^2}{2m_2(\lambda)}\frac{\partial F}{\partial z}\bigg|_{Z_{\mathrm{top}}^+},
\end{aligned} \tag{4}$$

where the + and − signs denote that the corresponding outward normal derivatives on the interface are defined for the matrix and the dot regions, respectively.

## 3. Discretization and matrix reduction methods

To discretize the model (1), we modify the disk discretization scheme described in [21] for which the grid points are shifted with a half mesh width in the radial direction. This setting avoids placing grid points on the natural axis and hence that the coefficients of the unknown scalars along the axial axis are cancelled out. Therefore, no pole conditions need to be imposed. Moreover, by using this discretization scheme, we can mathematically transform the resulting 3D eigenproblem into a set of independent 2D eigenproblems. Only several 2D eigenproblems are required to be solved for all possible bound states. This reduction dramatically reduce the computational cost without losing the accuracy. Nevertheless, the order of the energy

levels depends critically on the number of subsystems, i.e., on the partition number in the azimuthal direction.

To generate mesh points, the discretization scheme partitions the domain in the azimuthal direction uniformly. Since the wave functions change rapidly around the heterojunction, the scheme partitions the domain in the radial and axial directions in a nonuniform manner by adding more points around the heterojunction. More specifically, fine meshes with mesh length $\Delta r_f$ and $\Delta z_f$ are constructed around the heterojunction whereas larger mesh lengths $\Delta r_c$ ($\Delta r_f < \Delta r_c$) and $\Delta z_c$ ($\Delta z_f < \Delta z_c$) in other regions. Fig. 2 illustrates the discretization for a typical cross-section of the domain in the azimuth direction.

We then use the seven-point central finite difference method to discretize Eq. (1) at these grid points, i.e.,

$$\frac{-\hbar^2}{2m_\ell(\lambda)}\left(\frac{2F_{i+1,j,k}\Delta r_1 - 2F_{i,j,k}(\Delta r_1+\Delta r_2)+2F_{i-1,j,k}\Delta r_2}{(\Delta r_1+\Delta r_2)(\Delta r_1)(\Delta r_2)}+\frac{1}{r_i}\frac{F_{i+1,j,k}-F_{i-1,j,k}}{\Delta r_1+\Delta r_2}\right.$$
$$\left.+\frac{1}{r_i^2}\frac{F_{i,j+1,k}-2F_{i,j,k}+F_{i,j-1,k}}{(\Delta\theta)^2}+\frac{2F_{i,j,k+1}\Delta z_2 - 2F_{i,j,k}(\Delta z_1+\Delta z_2)+2F_{i,j,k-1}\Delta z_1}{(\Delta z_1+\Delta z_2)(\Delta z_1)(\Delta z_2)}\right)+c_\ell F_{i,j,k}=\lambda F_{i,j,k}, \tag{5}$$

where $F_{i,j,k}$ is an approximated value of function $F$ at the grid point $(r_i,\theta_j,z_k)$ for $\ell=1,2$, $i=1,\ldots,\rho$, $j=1,\ldots,\mu$, and $k=1,\ldots,\zeta$. The indices $\rho$, $\mu$, and $\zeta$ are grid point numbers in $r$, $\theta$, and $z$ directions, respectively. Here, $\Delta r_1$ and $\Delta r_2$ are left and right mesh lengths at the point along the radial direction representing either $\Delta r_c$ or $\Delta r_f$ according to the location of the point in the domain. Similarly, the mesh lengths along the axial direction $\Delta z_1$ and $\Delta z_2$ represent either $\Delta z_c$ or $\Delta z_f$. By letting $r_0=0$ and using the grid points, it can be seen that the coefficients of $F_{0,j,k}$ are zero. At the heterojunction, the interface conditions are approximated by regular two-point finite difference with the fine mesh size $\Delta r_f$ and $\Delta z_f$. Finally, the nodal values on the boundary of the domain are set to zero according to the Dirichlet conditions (3).

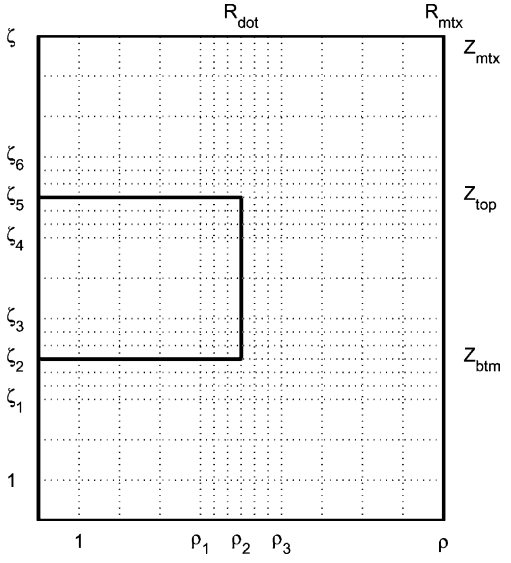


Fig. 2. Schema of the nonuniform discretization scheme of a 2D half plane. $R_{\rm dot}$ and $R_{\rm mtx}$ denote the radii of the dot and the matrix, respectively. $Z_{\rm btm}$ and $Z_{\rm top}$ denote the bottom and top of the dot. $Z_{\rm mtx}$ denotes the top of the matrix. Grid points are indexed from 1 to $\rho$ (1 to $\zeta$) in the radial (axial) coordinate. Note that fine meshes are used around the heterojunction.

These discrete equations can easily grow to an unduly large $\rho\mu\zeta$-by-$\rho\mu\zeta$ eigenvalue system as the sufficiently large number of grid points are required for numerical simulation of the model. Instead of solving the huge system in a straightforward manner (which is obviously infeasible in practical simulation), we devise a divide-and-conquer approach which is briefly described as follows. First of all, we observe that, for each $k = 1, \ldots, \zeta$, Eq. (5) and the grid points represent a subsystem corresponding to a slice of horizontal disk (in polar coordinates) and can be assembled as follows:

$$\begin{bmatrix} T_1(\lambda) & E_1(\lambda) & & & \\ B_2(\lambda) & T_2(\lambda) & E_2(\lambda) & & \\ & \ddots & \ddots & \ddots & \\ & & B_{\zeta-1}(\lambda) & T_{\zeta-1}(\lambda) & E_{\zeta-1}(\lambda) \\ & & & B_\zeta(\lambda) & T_\zeta(\lambda) \end{bmatrix} \begin{bmatrix} F_{:,:,1} \\ F_{:,:,2} \\ \vdots \\ F_{:,:,\zeta-1} \\ F_{:,:,\zeta} \end{bmatrix} = D(\lambda) \begin{bmatrix} F_{:,:,1} \\ F_{:,:,2} \\ \vdots \\ F_{:,:,\zeta-1} \\ F_{:,:,\zeta} \end{bmatrix}, \tag{6}$$

where $F_{:,:,k}$ is an unknown vector corresponding to some disk and the matrices $B_k$, $E_k$, and $T_k$ are defined by

$$B_k = \operatorname{diag}\left[B_{1,k}, \ldots, B_{\rho,k}\right] \in \mathbb{R}^{\rho\mu\times\rho\mu},$$

$$E_k = \operatorname{diag}\left[E_{1,k}, \ldots, E_{\rho,k}\right] \in \mathbb{R}^{\rho\mu\times\rho\mu},$$

$$T_k = \begin{bmatrix} S_{1,k} & H_{1,k} & & & 0 \\ G_{2,k} & S_{2,k} & H_{2,k} & & \\ & \ddots & \ddots & \ddots & \\ & & G_{\rho-1,k} & S_{\rho-1,k} & H_{\rho-1,k} \\ 0 & & & G_{\rho,k} & S_{\rho,k} \end{bmatrix} \in \mathbb{R}^{\rho\mu\times\rho\mu}. \tag{7}$$

Here, the matrices $S_{i,k}$, $G_{i,k}$, $H_{i,k}$, $B_{i,k}$, and $E_{i,k}$ are defined by either one of the following two cases.

*Case* (i). If the matrices do not involve the interface,

$$S_{i,k} = -\frac{\hbar^2}{2m_\ell(\lambda)} \begin{bmatrix} \eta_{i,k} - 2\beta_i & \beta_i & & & & \beta_i \\ \beta_i & \eta_{i,k} - 2\beta_i & \beta_i & & & \\ & \ddots & \ddots & \ddots & & \\ & & \beta_i & \eta_{i,k} - 2\beta_i & \beta_i & \\ \beta_i & & & \beta_i & \eta_{i,k} - 2\beta_i \end{bmatrix}, \tag{8}$$

$$G_{i,k} = -\frac{\hbar^2}{2m_\ell(\lambda)}\varphi_i \mathbf{I}_\mu, \quad H_{i,k} = -\frac{\hbar^2}{2m_\ell(\lambda)}\alpha_i \mathbf{I}_\mu,$$

$$B_{i,k} = -\frac{\hbar^2}{2m_\ell(\lambda)}\varrho_k \mathbf{I}_\mu, \quad E_{i,k} = -\frac{\hbar^2}{2m_\ell(\lambda)}\tau_k \mathbf{I}_\mu,$$

where $S_{i,k}$, $G_{i,k}$, $H_{i,k}$, $B_{i,k}$, and $E_{i,k}$ belong to $\mathbb{R}^{\mu\times\mu}$, $\beta_i = \mu^2/(r_i^2\pi^2)$ with

$$r_i = \begin{cases} (i - 1/2)\Delta r_c & \text{if } 1 \leqslant i \leqslant \rho_1, \\ r_{\rho_1} + (i - \rho_1)\Delta r_f & \text{if } \rho_1 + 1 \leqslant i \leqslant \rho_3, \\ r_{\rho_3} + (i - \rho_3)\Delta r_c & \text{if } \rho_3 + 1 \leqslant i \leqslant \rho, \end{cases}$$

where $\eta_{i,k}$, $\varphi_i$, $\alpha_i$, $\varrho_k$, and $\tau_k$ are constants defined in Tables 1 and 2.

Table 1
Definition of the coefficients $\varrho_k$ and $\tau_k$

| $k$ | $1,\ldots,\zeta_1-1$ | $\zeta_1$ | $\zeta_1+1,\ldots,\zeta_3-1$ |
|---|---|---|---|
| $\varrho_k$ | $1/(\Delta z_c)^2$ | $2/[(\Delta z_c+\Delta z_f)\Delta z_c]$ | $1/(\Delta z_f)^2$ |
| $\tau_k$ | $1/(\Delta z_c)^2$ | $2/[(\Delta z_c+\Delta z_f)\Delta z_f]$ | $1/(\Delta z_f)^2$ |
| $\kappa_k$ | $2/(\Delta z_c)^2$ | $2/(\Delta z_c\Delta z_f)$ | $2/(\Delta z_f)^2$ |
| $k$ | $\zeta_3$ | $\zeta_3+1,\ldots,\zeta_4-1$ | $\zeta_4$ |
| $\varrho_k$ | $2/[(\Delta z_c+\Delta z_f)\Delta z_f]$ | $1/(\Delta z_c)^2$ | $2/[(\Delta z_c+\Delta z_f)\Delta z_c]$ |
| $\tau_k$ | $2/[(\Delta z_c+\Delta z_f)\Delta z_c]$ | $1/(\Delta z_c)^2$ | $2/[(\Delta z_c+\Delta z_f)\Delta z_f]$ |
| $\kappa_k$ | $2/(\Delta z_c\Delta z_f)$ | $2/(\Delta z_c)^2$ | $2/(\Delta z_c\Delta z_f)$ |
| $k$ | $\zeta_4+1,\ldots,\zeta_6-1$ | $\zeta_6$ | $\zeta_6+1,\ldots,\zeta$ |
| $\varrho_k$ | $1/(\Delta z_f)^2$ | $2/[(\Delta z_c+\Delta z_f)\Delta z_f]$ | $1/(\Delta z_c)^2$ |
| $\tau_k$ | $1/(\Delta z_f)^2$ | $2/[(\Delta z_c+\Delta z_f)\Delta z_c]$ | $1/(\Delta z_c)^2$ |
| $\kappa_k$ | $2/(\Delta z_f)^2$ | $2/(\Delta z_c\Delta z_f)$ | $2/(\Delta z_c)^2$ |

The constants $\kappa_k$ are used to define $\eta_{i,k}$ in Table 2. See Fig. 2 for the definition of mesh point indices $\zeta_1$–$\zeta_6$ and $\zeta$.

Table 2
Definition of the coefficients $\varphi_i, \alpha_i$ and $\eta_{i,k}$

| $i$ | $1,\ldots,\rho_1-1$ | $\rho_1$ |
|---|---|---|
| $\varphi_i$ | $1/(\Delta r_c)^2-1/(2r_i\Delta r_c)$ | $2/[(\Delta r_c+\Delta r_f)\Delta r_c]-1/[r_{\rho_1}(\Delta r_c+\Delta r_f)]$ |
| $\alpha_i$ | $1/(\Delta r_c)^2+1/(2r_i\Delta r_c)$ | $2/[(\Delta r_c+\Delta r_f)\Delta r_f]+1/[r_{\rho_1}(\Delta r_c+\Delta r_f)]$ |
| $\eta_{i,k}$ | $-2/(\Delta r_c)^2-\kappa_k$ | $-2/(\Delta r_c\Delta r_f)-\kappa_k$ |
| $i$ | $\rho_1+1,\ldots,\rho_3-1$ | $\rho_3$ |
| $\varphi_i$ | $1/(\Delta r_f)^2-1/(2r_i\Delta r_f)$ | $2/[(\Delta r_c+\Delta r_f)\Delta r_f]-1/[r_{\rho_3}(\Delta r_c+\Delta r_f)]$ |
| $\alpha_i$ | $1/(\Delta r_f)^2+1/(2r_i\Delta r_f)$ | $2/[(\Delta r_c+\Delta r_f)\Delta r_c]+1/[r_{\rho_3}(\Delta r_c+\Delta r_f)]$ |
| $\eta_{i,k}$ | $-2/(\Delta r_f)^2-\kappa_k$ | $-2/(\Delta r_c\Delta r_f)-\kappa_k$ |
| $i$ | $\rho_3+1,,\ldots,\rho-1$ | $\rho$ |
| $\varphi_i$ | $1/(\Delta r_c)^2-1/(2r_i\Delta r_c)$ | $1/(\Delta r_c)^2-1/(2r_i\Delta r_c)$ |
| $\alpha_i$ | $1/(\Delta r_c)^2+1/(2r_i\Delta r_c)$ | 0 |
| $\eta_{i,k}$ | $-2/(\Delta r_c)^2-\kappa_k$ | $-2/(\Delta r_c)^2-\kappa_k$ |

Note that the constants $\kappa_k$ are defined in Table 1. See Fig. 2 for the definition of mesh point indices $\rho_1$, $\rho_2$, $\rho_3$, and $\rho$.

*Case* (ii). Otherwise, we have

$$S_{i,k}=\left(\frac{\hbar^2}{2m_1(\lambda)}+\frac{\hbar^2}{2m_2(\lambda)}\right)\mathbf{I}_\mu \tag{9}$$

and the matrices $B_{i,k}$, $E_{i,k}$, $G_{i,k}$, $H_{i,k}$ are defined by either one of the three cases shown in Table 3.

Finally, the block diagonal matrix $D$ is defined as

$$D=\operatorname{diag}\Big[(\lambda-c_2)\mathbf{I}_{\rho\mu},\ldots,(\lambda-c_2)\mathbf{I}_{\rho\mu},\tilde{I},\hat{I},\ldots,\hat{I},\tilde{I},(\lambda-c_2)\mathbf{I}_{\rho\mu},\ldots,(\lambda-c_2)\mathbf{I}_{\rho\mu}\Big],$$

Table 3
Possible choices of matrices $B_{i,k}$, $E_{i,k}$, $G_{i,k}$, $H_{i,k}$ while the mesh points involve interface

| Interface type | $B_{i,k}$ | $E_{i,k}$ | $G_{i,k}$ | $H_{i,k}$ |
|---|---|---|---|---|
| Sidewall | $\mathbf{0}_\mu$ | $\mathbf{0}_\mu$ | $(-\hbar^2/2m_1(\lambda))\mathbf{I}_\mu$ | $(-\hbar^2/2m_2(\lambda))\mathbf{I}_\mu$ |
| Top | $(-\hbar^2/2m_1(\lambda))\mathbf{I}_\mu$ | $(-\hbar^2/2m_2(\lambda))\mathbf{I}_\mu$ | $\mathbf{0}_\mu$ | $\mathbf{0}_\mu$ |
| Bottom | $(-\hbar^2/2m_2(\lambda))\mathbf{I}_\mu$ | $(-\hbar^2/2m_1(\lambda))\mathbf{I}_\mu$ | $\mathbf{0}_\mu$ | $\mathbf{0}_\mu$ |

where

$$\tilde{I} = \operatorname{diag}\left[\mathbf{0}_{\rho_2\mu},\ (\lambda - c_2)\mathbf{I}_{(\rho-\rho_2)\mu}\right] \in \mathbb{R}^{\rho\mu\times\rho\mu},$$

and

$$\hat{I} = \operatorname{diag}\left[(\lambda - c_1)\mathbf{I}_{(\rho_2-1)\mu},\ \mathbf{0}_{\mu},\ (\lambda - c_2)\mathbf{I}_{(\rho-\rho_2)\mu}\right] \in \mathbb{R}^{\rho\mu\times\rho\mu}.$$

The coefficient matrix in (6) is then transformed to a block diagonal matrix by the following steps.

(i) *Block diagonalizing the coefficient matrix in (6).*

The matrices $S_{i,k}$ defined in (8) can be written in the form of

$$S_{i,k} = \eta_{i,k} I - 2\beta_i \mathscr{C},$$

where the matrix $\mathscr{C}$ is symmetric and circulant. As shown in [22], a symmetric and circulant matrix can be diagonalized by using the Fourier matrix transformation which is also a similarity transformation. That is, there exists an orthonormal matrix $\widehat{W} \in \mathbb{R}^{\mu\times\mu}$ such that $\widehat{W}^{\mathrm{T}}\mathscr{C}\widehat{W}$ is diagonal. Moreover, since the matrices $G_{i,k}$, $H_{i,k}$, $B_{i,k}$, and $E_{i,k}$ are multipliers of identity matrix, they remain unchanged through multiplications of the orthonormal matrix $\widehat{W}^{\mathrm{T}}$ from left and $\widehat{W}$ from right. Therefore, by letting

$$W = \operatorname{diag}[\widehat{W}, \ldots, \widehat{W}], \tag{10}$$

we see that $W^{\mathrm{T}}T_kW$ contains nonzeros in the main diagonal, the $\mu$th superdiagonal, and the $\mu$th subdiagonal. The matrix $W^{\mathrm{T}}T_kW$ can be further transformed to a block diagonal matrix by suitable permutations. That is, there exists a permutation matrix $\Pi_1 \in \mathbb{R}^{\rho\mu\times\rho\mu}$ such that

$$\Pi_1^{\mathrm{T}} W^{\mathrm{T}} T_k W \Pi_1 = diag\left[T_{1,k}, \ldots, T_{\mu,k}\right], \tag{11}$$

where $T_{j,k}$ are $\rho$-by-$\rho$ tridiagonal matrices for $j = 1, \ldots, \mu$.

Applying

$$W_{\Pi D} = \operatorname{diag}[W\Pi_1, \ldots, W\Pi_1],$$

Eq. (11), and a suitable permutation $\Pi_2 \in \mathbb{R}^{\rho\mu\zeta\times\rho\mu\zeta}$ to the coefficient matrix in (6), we obtain

$$\Pi_2^{\mathrm{T}} W_{\Pi D}^{\mathrm{T}} \begin{bmatrix} T_1 & E_1 & & \\ B_2 & T_2 & \ddots & \\ & \ddots & \ddots & E_{\zeta-1} \\ & & B_\zeta & T_\zeta \end{bmatrix} W_{\Pi D}\Pi_2 = \Pi_2^{\mathrm{T}} \begin{bmatrix} \operatorname{diag}[T_{1,1}, \ldots, T_{\mu,1}] & E_1 & & \\ & \ddots & \ddots & \\ B_2 & \ddots & \ddots & E_{\zeta-1} \\ & & B_\zeta & \operatorname{diag}[T_{1,\zeta}, \ldots, T_{\mu,\zeta}] \end{bmatrix} \Pi_2$$

$$= \begin{bmatrix} \widetilde{T}_1 & & \\ & \ddots & \\ & & \widetilde{T}_\mu \end{bmatrix}, \tag{12}$$

where

$$\widetilde{T}_j = \begin{bmatrix} T_{j,1} & \widetilde{E}_1 & & & \\ \widetilde{B}_2 & T_{j,2} & \widetilde{E}_2 & & \\ & \ddots & \ddots & \ddots & \\ & & \widetilde{B}_{\zeta-1} & T_{j,\zeta-1} & \widetilde{E}_{\zeta-1} \\ & & & \widetilde{B}_\zeta & T_{j,\zeta} \end{bmatrix} \in \mathbb{R}^{\rho\zeta\times\rho\zeta} \quad \text{for } j = 1, \ldots, \mu,$$

and $\widetilde{B}_i$, $\widetilde{E}_i$ are $\rho$-by-$\rho$ diagonal matrices. In other words, the coefficient matrix is now transformed to a block diagonal matrix.

(ii) *Reordering the unknown eigenvector.*

We shall now transform the eigenvector in (6)accordingly. To do so, we simply define

$$[\widetilde{F}_1, \ldots, \widetilde{F}_\mu]^{\mathrm{T}} = \Pi_2^{\mathrm{T}} W_{\Pi D}^{\mathrm{T}} [F_{:,:,1}, \ldots, F_{:,:,\zeta}]^{\mathrm{T}}, \tag{13}$$

where $\widetilde{F}_j \in \mathbb{R}^{\rho\zeta\times 1}$ for $j = 1$ to $\mu$ and $F_{:,:,k} \in \mathbb{R}^{\rho\mu\times 1}$ for $k = 1$ to $\zeta$. In other words, the unknowns in the same vertical slice of the domain are grouped together in Eq. (13). For clarity, the effect of the permutations $\Pi_1 \in \mathbb{R}^{\rho\mu\times\rho\mu}$ and $\Pi_2 \in \mathbb{R}^{\rho\mu\zeta\times\rho\mu\zeta}$ are shown as follows:

$$\begin{aligned}&\left[F_{1,1,k}, \ldots, F_{1,\mu,k}, F_{2,1,k}, \ldots, F_{2,\mu,k}, \ldots, F_{\rho,1,k}, \ldots, F_{\rho,\mu,k}\right]\Pi_1\\ &\quad = \left[F_{1,1,k}, \ldots, F_{\rho,1,k}, F_{1,2,k}, \ldots, F_{\rho,2,k}, \ldots, F_{1,\mu,k}, \ldots, F_{\rho,\mu,k}\right],\end{aligned}$$

and

$$\left[F_{:,:,1}^{\mathrm{T}}, \ldots, F_{:,:,\zeta}^{\mathrm{T}}\right]\mathrm{diag}[\Pi_1, \ldots, \Pi_1]\Pi_2 = \left[F_{:,1,:}^{\mathrm{T}}, \ldots, F_{:,\mu,:}^{\mathrm{T}}\right]$$

where

$$F_{:,j,:} = [F_{1,j,1}, \ldots, F_{\rho,j,1}, F_{1,j,2}, \ldots, F_{\rho,j,2}, \ldots, F_{1,j,\zeta}, \ldots, F_{\rho,j,\zeta}]^{\mathrm{T}}.$$

Finally, the diagonal matrix $D$ in Eq. (6) is reordered as

$$(\Pi_2^{\mathrm{T}} W_{\Pi D}^{\mathrm{T}}) D (W_{\Pi D}\Pi_2) = \Pi_2^{\mathrm{T}} D \Pi_2 = \mathrm{diag}[\widetilde{D}_1, \ldots, \widetilde{D}_\mu], \tag{14}$$

where $\widetilde{D}_j$ is a $\rho\zeta$-by-$\rho\zeta$ diagonal matrix for $j = 1, \ldots, \mu$.

(iii) *Transforming Eq. (6) into a block diagonal system.*

Using Eqs. (12)–(14), the $\rho\mu\zeta$-by-$\rho\mu\zeta$ eigenvalue system (6) can be transformed to the following form:

$$\begin{bmatrix} \widetilde{T}_1 & & \\ & \ddots & \\ & & \widetilde{T}_\mu \end{bmatrix} \begin{bmatrix} \widetilde{F}_1 \\ \vdots \\ \widetilde{F}_\mu \end{bmatrix} = \begin{bmatrix} \widetilde{D}_1 & & \\ & \ddots & \\ & & \widetilde{D}_\mu \end{bmatrix} \begin{bmatrix} \widetilde{F}_1 \\ \vdots \\ \widetilde{F}_\mu \end{bmatrix}. \tag{15}$$

Note that $\widetilde{T}_{\mu-j+1} = \widetilde{T}_j$, and $\widetilde{D}_{\mu-j+1} = \widetilde{D}_j$ for $j = 2, \ldots, \mu/2$ (or $(\mu-1)/2$, if $\mu$ is odd).

In short, we have successfully divided the large $\rho\mu\zeta$-by-$\rho\mu\zeta$ 3D eigenvalue problem (6) into $\mu$ independent $\rho\zeta$-by-$\rho\zeta$ 2D subsystems

$$\widetilde{T}_j \widetilde{F}_j = \widetilde{D}_j \widetilde{F}_j, \tag{16}$$

for $j = 1, \ldots, \mu$.

## 4. Cubic Jacobi–Davidson and deflation methods

We now focus on solving each individual subsystem in (16), which can be rewritten as a generalized eigenvalue problem

$$\mathbf{G}(\lambda)\mathbf{F} = \mathbf{D}(\lambda)\mathbf{F}, \tag{17}$$

where $\mathbf{G}(\lambda)$ is a $\rho\zeta$-by-$\rho\zeta$ matrix, $\mathbf{F}$ is the unknown vector, and $\mathbf{D}(\lambda)$ is the corresponding diagonal matrix. Note that the entries of the matrix $\mathbf{G}(\lambda)$ involve the eigenvalues $\lambda$ in the denominator originated from the mass Eq. (2). We first reformulate the problem to the following form:

$$\mathbf{A}(\lambda)\mathbf{F} = (\lambda^3 A_3 + \lambda^2 A_2 + \lambda A_1 + A_0)\mathbf{F} = 0 \tag{18}$$

by multiplying the common denominator in the right-hand side of the mass equation to (17). Here the matrices $A_1$, $A_2$, and $A_3$ are independent of $\lambda$ and are obtained by a linear combination of various parts of $\mathbf{G}(\lambda)$ and $\mathbf{D}(\lambda)$.

This eigenvalue problem is of cubic type for which numerical methods are rarely available in the literature when compared with, for instance, the quadratic eigenvalue problems. We propose here two methods for this cubic eigenvalue problem. For computing the smallest eigenpair, the first method is a generalization of the quadratic Jacobi–Davidson method described, for example, in [23, Section 9.2]. The method simply replaces the quadratic matrix polynomial by the cubic matrix polynomial and replaces the iteration indices $0, 1, 2$ by $0, 1, 2, 3$ with some modifications on the deflation transformations to be described below.

To find the successive eigenpairs for linear eigenvalue problems, the Jacobi–Davidson method combined with the implicit deflation technique based on Schur forms (see e.g. [24, Sections 4.7 and 8.4]) performs well. However, it is not clear how to incorporate the deflation technique with the quadratic or high-order eigenvalue problems. The main reason is that Schur forms do not exist for a quadratic or a polynomial pencil in general. To overcome the difficulty, a locking and restarting quadratic eigensolver is recently proposed in [25]. The locking and restarting strategy is based on a partial Schur form of the linearized problem. It essentially locks the desired eigenvalues in a reduced quadratic pencil by an equivalence projection. For the cubic problem (18), the corresponding linearized problem is

$$\begin{bmatrix} 0 & I & 0 \\ 0 & 0 & I \\ A_0 & A_1 & A_2 \end{bmatrix} \begin{bmatrix} \mathbf{F} \\ \lambda\mathbf{F} \\ \lambda^2\mathbf{F} \end{bmatrix} = \lambda \begin{bmatrix} I & 0 & 0 \\ 0 & I & 0 \\ 0 & 0 & -A_3 \end{bmatrix} \begin{bmatrix} \mathbf{F} \\ \lambda\mathbf{F} \\ \lambda^2\mathbf{F} \end{bmatrix}. \tag{19}$$

Our next method is an explicit nonequivalence low-rank deflation method together with the locking and restarting strategy using the partial Schur form of this linearized problem. Once the smallest eigenvalue is obtained, it is then transformed to infinity by the deflation scheme, while all other eigenvalues remain unchanged. The next successive eigenvalue thus becomes the smallest eigenvalue of the newly transformed cubic eigenvalue problem which is then again solved by the cubic Jacobi–Davidson method. Only several transformations are needed for determining the corresponding eigenvectors. We elaborate the explicit nonequivalence deflation as follows. Let $(\Lambda_1, Y_1) \in \mathbb{R}^{r\times r} \times \mathbb{R}^{n\times r}$ with $Y_1^{\mathrm{T}} Y_1 = I_r$ be an eigenmatrix pair of $\mathbf{A}(\lambda)$, i.e.,

$$A_3 Y_1 \Lambda_1^3 + A_2 Y_1 \Lambda_1^2 + A_1 Y_1 \Lambda_1 + A_0 Y_1 = 0, \tag{20}$$

where $n$ is the dimension of the eigenvalue problem and the scalar $r \ll n$. Suppose that $0 \notin \sigma(\Lambda_1)$ where $\sigma(\Lambda_1)$ denotes the spectrum of $\Lambda_1$. The new deflated cubic eigenvalue problem is defined as

$$\widetilde{\mathbf{A}}(\lambda)\mathbf{F} = (\lambda^3 \tilde{A}_3 + \lambda^2 \tilde{A}_2 + \lambda \tilde{A}_1 + \tilde{A}_0)\mathbf{F} = 0, \tag{21}$$

where

$$\begin{cases} \tilde{A}_0 = A_0, \\ \tilde{A}_1 = A_1 - (A_1 Y_1 Y_1^{\mathrm{T}} + A_2 Y_1 \Lambda_1 Y_1^{\mathrm{T}} + A_3 Y_1 \Lambda_1^2 Y_1^{\mathrm{T}}), \\ \tilde{A}_2 = A_2 - (A_2 Y_1 Y_1^{\mathrm{T}} + A_3 Y_1 \Lambda_1 Y_1^{\mathrm{T}}), \\ \tilde{A}_3 = A_3 - A_3 Y_1 Y_1^{\mathrm{T}}. \end{cases} \tag{22}$$

As stated in the following two theorems, the scheme described in (21) and (22) deflates the computed eigenvalues of $\mathbf{A}(\lambda)$, i.e., $\sigma(\Lambda_1)$, while all other unknown eigenvalues of $\mathbf{A}(\lambda)$ remain unchanged. By iteratively updating the matrix $\widetilde{\mathbf{A}}(\lambda)$, all desired eigenpairs can thus be successively computed. Note that a proof of the theorems can be readily extended from that of [26].

**Theorem 1.** *Let* $(\Lambda_1, Y_1) \in \mathbb{R}^{r\times r} \times \mathbb{R}^{n\times r}$ *with* $Y_1^{\mathrm{T}} Y_1 = I_r$ *be an eigenmatrix pair of* $\mathbf{A}(\lambda)$ *as in* (20). *Then the new deflated cubic polynomial* $\widetilde{\mathbf{A}}(\lambda)$ *defined by* (21) and (22) *has the same eigenvalues as those of* $\mathbf{A}(\lambda)$ *except that r eigenvalues of* $\Lambda_1$ *are replaced by r infinity eigenvalues, i.e.,* $(\sigma(\mathbf{A}(\lambda)) \setminus \sigma(\Lambda_1)) \cup \{\infty\} = \sigma(\widetilde{\mathbf{A}}(\lambda))$.

**Theorem 2.** *Suppose that* $\lambda_2 \notin \sigma(\Lambda_1)$ *and* $(\lambda_2, y_2)$ *is an eigenpair of* $\mathbf{A}(\lambda)$.
*Define*

$$T(\lambda) = I_n - \lambda Y_1 \Lambda_1^{-1} Y_1^{\mathrm{T}} \tag{23}$$

*and*

$$\tilde{y}_2 = (I_n - \lambda_2 Y_1 \Lambda_1^{-1} Y_1^{\mathrm{T}}) y_2 = T(\lambda_2) y_2. \tag{24}$$

*Then* $(\lambda_2, \tilde{y}_2)$ *is an eigenpair of* $\widetilde{\mathbf{A}}(\lambda)$.

Now we can compute the successive eigenpairs by repeatedly applying the explicit nonequivalence deflation scheme and the cubic Jacobi–Davidson method straightforwardly extended from the quadratic version presented in [24]. In the first part of the cubic Jacobi–Davidson iteration, the approximate Ritz pair of the projected polynomial problem $(V^{\mathrm{T}}\mathbf{A}(\theta)V)s = 0$ is solved. The matrix $V \in \mathbb{R}^{n\times q}$, $q < n$, is the search subspace. Then we compute the approximate eigenvector $u = Vs$, the residual $r = \mathbf{A}(\theta)u$, and the vector $p = \mathbf{A}'(\theta)u$. Secondly, we solve approximately the correction equation

$$\left(I - \frac{pu^*}{u^*p}\right)\mathbf{A}(\theta)(I - uu^*)t = -r \tag{25}$$

by computing

$$t = -M_A^{-1}r + \varepsilon M_A^{-1}p \quad \text{with } \varepsilon = \frac{u^*M_A^{-1}r}{u^*M_A^{-1}p}. \tag{26}$$

The matrix $M_A$ is a preconditioner of $\mathbf{A}(\theta)$. In the SSOR preconditioning scheme [27],

$$\mathbf{A}(\theta) \approx M_{\mathbf{A}} = (D - \omega L)D^{-1}(D - \omega U),$$

where $\omega$ is a scalar, $\mathbf{A}(\theta) = D - L - U$ with $D = \mathrm{diag}(\mathbf{A}(\theta))$, $L$ and $U$ are strictly lower and upper triangular of $\mathbf{A}(\theta)$. However, this straightforward cubic Jacobi–Davidson approach is not efficient since it is associated with the deflated system (21) and (22). As more and more eigenpairs to be determined, the number of deflation transformations with low rank updates (21) and (22) would increase.

Fortunately, we can eliminate the deflation transformations to reduce computational costs by the following observation. If we directly extend the quadratic Jacobi–Davidson method to fit the cubic polynomial, the computations of the vector $\tilde{r}$ ($\tilde{r} = \widetilde{\mathbf{A}}(\theta)\tilde{u}$), the vector $\tilde{p}$ ($\tilde{p} = \widetilde{\mathbf{A}}'(\theta)\tilde{u}$), and the parameter $\varepsilon$ will be affected by the deflation transformations. However, by using the definition of $\widetilde{\mathbf{A}}(\lambda)$, we have

$$\widetilde{\mathbf{A}}(\theta)T(\theta) = A(\theta) \tag{27}$$

and

$$\widetilde{\mathbf{A}}'(\theta)T(\theta) = \mathbf{A}'(\theta) - [A_3 Y_1(\Lambda_1^2 + \theta\Lambda_1 + \theta^2 I_r)Y_1^{\mathrm{T}} + A_2 Y_1(\Lambda_1 + \theta I_r)Y_1^{\mathrm{T}} + A_1 Y_1 Y_1^{\mathrm{T}}], \tag{28}$$

where $(\theta, \tilde{u})$ is the approximate Ritz pair of $\widetilde{\mathbf{A}}(\lambda)$. Besides, since Theorem 2 suggests that

$$u = T(\theta)^{-1}\tilde{u}, \tag{29}$$

we can replace $\tilde{u}$ by $T(\theta)u$ in the computation of $\tilde{r}$ and $\tilde{p}$ so that

$$\tilde{r} = \mathbf{A}(\theta)u \tag{30}$$

and

$$\tilde{p} = \mathbf{A}'(\theta)u - \left[A_3 Y_1 \left(\Lambda_1^2 + \theta\Lambda_1 + \theta^2 I_r\right) Y_1^{\mathrm{T}} + A_2 Y_1 (\Lambda_1 + \theta I_r) Y_1^{\mathrm{T}} + A_1 Y_1 Y_1^{\mathrm{T}}\right] u. \tag{31}$$

In other words, the computations of $\tilde{r}$ and $\tilde{p}$ involve only the original system, rather than the deflated system.

By (25), (26), (30), and (31), we compute

$$t = -M_A^{-1}\tilde{r} + \varepsilon M_A^{-1}\tilde{p} \quad \text{with } \varepsilon = \frac{u^* M_A^{-1}\tilde{r}}{u^* M_A^{-1}\tilde{p}}$$

for the correction equation

$$(I - (\tilde{p}u^*)/(u^*\tilde{p}))\mathbf{A}(\theta)(I - uu^*)t = -\tilde{r}.$$

We then obtain a more efficient cubic Jacobi–Davidson method that no deflated system $\widetilde{\mathbf{A}}(\theta)$ is involved. This solution process is repeated until all bound state eigenpairs are found. Algorithms 3 and 4 summarize these ideas by dropping the tilde notation (˜) since the computations involve the original, not the deflated, space only.

**Algorithm 3.** Cubic Jacobi–Davidson method with explicit deflation.

*Step* (1) *Choose an n*-by-*m orthonormal matrix V*

*Step* (2) *For* $i = 0, 1, 2, 3$

*Compute* $W_i = A_i V$ *and* $M_i = V^* W_i$

*Step* (3) *Iterate until convergence*

(3.1) *Compute the eigenpairs* $(\theta, s)$ *of* $(\theta^3 M_3 + \theta^2 M_2 + \theta M_1 + M_0)s = 0$

(3.2) *Select the desired eigenpair* $(\theta, s)$ *with* $\|s\|_2 = 1$.

(3.3) *Compute* $u = Vs$, $r = \mathbf{A}(\theta)u$, *and p by Eq.* (31)

(3.4) *If*$(\|r\|_2 < \varepsilon)$, $\lambda = \theta$, $x = u$, *Quit*

(3.5) *Compute* $t = -M_A^{-1}r + \varepsilon M_A^{-1}p$*where* $\varepsilon = \frac{u^* M_A^{-1} r}{u^* M_A^{-1} p}$

(3.6) *Orthogonalize t against V*, $v = t/\|t\|_2$.

(3.7) *For* $i = 0, 1, 2, 3$

*Compute* $w_i = A_i v$, $M_i = \begin{bmatrix} M_i & V^* w_i \\ v^* W_i & v^* w_i \end{bmatrix}$, $W_i = [W_i, w_i]$

(3.8) *Expand* $V = [V, v]$

*Step* (4) *Output* $(\theta, u)$ *as the computed eigenpair*

**Algorithm 4.** The main algorithm.

*Step* (0) *Given* $\mathbf{A}(\lambda) = \lambda^3 A_3 + \lambda^2 A_2 + \lambda A_1 + A_0$.

*Step* (1) *Initialize* $i = 0$. *Let* $\Lambda_1$ *and* $Y_1$ *be empty sets.*

*Step* (2) *Solve the ith deflated system* (21) *with* (22) *by* Algorithm 3 *to obtain the eigenpair* $(\lambda_i, \mathbf{F}_i)$.

*Step* (3) *Output the ith smallest positive eigenvalue* $\lambda_i$ and $\mathbf{F}_i$

*Step* (4) *If* (*no more eigenpair is needed*) *then Stop*; *Otherwise*

(4.1) *Update* $\Lambda_1$ *and* $Y_1$ *by orthogonalizing* $\mathbf{F}_i$ *against current* $Y_1$, *normalizing* $\mathbf{F}_i = \frac{\mathbf{F}_i}{\|\mathbf{F}_i\|}$, *and then expanding* $Y_1 = [Y_1, \mathbf{F}_i]$,

(4.2) *Let* $i = i + 1$,

(4.3) *Goto Step* (2)

## 5. Numerical results

As a typical example, we provide here some numerical and graphical results of computed energy levels and corresponding wave functions of the model with the diameter and the height being 12 and 2 nm, respectively, for the QD and being 72 and 12 nm for the matrix. The QD size is chosen so that it is approximately comparable with that of the experimental model presented in [28] and the nonparabolic effect of the band structure is significant [29].

For our numerical experiments, the algorithms have been implemented by Fortran 90 programming language. All numerical tests were performed on a Compaq AlphaServer DS20E workstation equipped with 667 MHz CPU and one gigabytes main memory. The operating system running on the machine is Compaq Tru64 UNIX version 5.0. The timing results are in seconds. The iterative processes of Algorithm 3 were terminated when the residual of Eq. (18) is less than $1.0 \times 10^{-8}$.

The first part of numerical results illustrates one of important issues in dealing with semiconductor heterostructures, namely, the interface problem. Note that the two-point finite difference approximation of the interface conditions is of linear order. Uniform and nonuniform meshes are both considered.

*Case* 1. Uniform meshes: $\Delta r_f = \Delta r_c = \Delta z_f = \Delta z_c = 0.1$, 0.05, or 0.025 nm. The matrix size of the resulting systems is 43078, 172558, or 690718, respectively, as shown on the dashed line in Fig. 3. The computed ground state energies increase to 0.1066.

*Case* 2. Nonuniform meshes: $\Delta r_f = \mathsf{ref\_ratio} \times \Delta r_c$, $\Delta z_f = \mathsf{ref\_ratio} \times \Delta z_c$, $\Delta r_c = \Delta z_c = 0.1$, 0.05, or 0.025 nm, $\mathsf{ref\_ratio} = 1/5$.

*Case* 3. Nonuniform meshes: Same as Case 2 except that $\mathsf{ref\_ratio} = 1/10$. All of the corresponding ground state energies converge to an approximate value 0.1091. Obviously, the uniform case is not efficient at all as indicated by the comparison between the approximated energies 0.1066 and 0.1091 in correspondence with the matrix sizes of 690718 and 751900. Moreover, although the mesh around the interface is

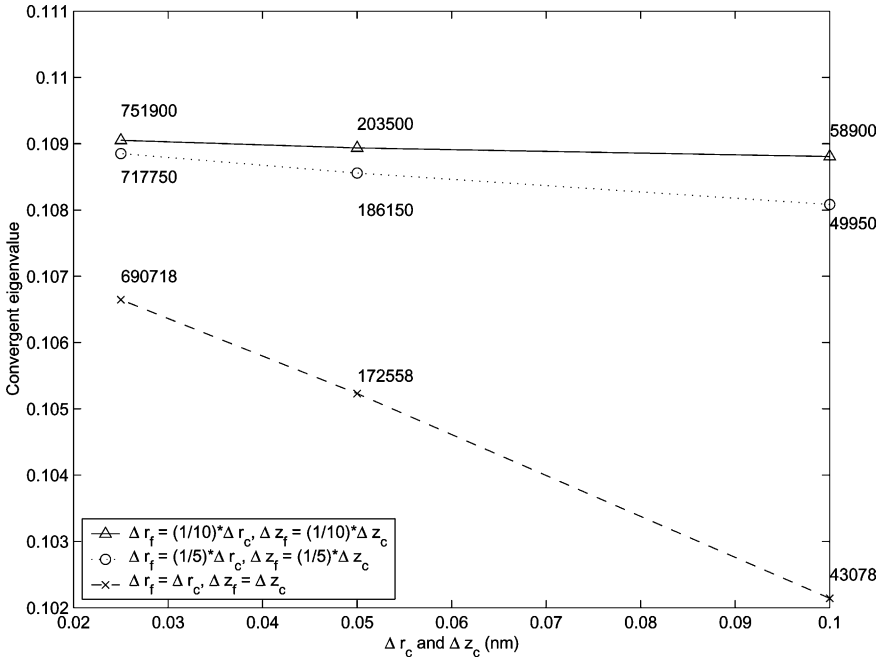


Fig. 3. The effect of nonuniform meshes. Various coarse mesh lengths and refinement schemes are used. The size of resulting matrix ($\rho \times \zeta$) are inscribed next to the eigenvalue data.

doubly refined from that of Case 2 to Case 3, the value is improved only slightly from 0.1089 to 0.1091. We conclude that advanced numerical treatments such as higher-order approximation, unstructured and adaptive mesh refinement, and error estimation, on the interface problem remain to be explored in the future development for modelling semiconductor heterostructures.

The second part of our numerical results is to show that the methods proposed here can attain bound states as many as possible within the confinement potential 0.35. The nonuniform mesh of Case 3 with $\Delta r_f = \frac{1}{10}\Delta r_c$ is used in what follows so that the computed eigenvalues are accurate up to three significant digits. An important factor for this part of results is the partitioning in the azimuthal direction, i.e., the number of partitions $\mu$. For this, the results are organized into the following two subcases.

*Subcase* 3.1. $\mu = 360$, $\Delta r_c = 0.040$ nm and $\Delta r_f = 0.004$ nm. The matrix size of the resulting 3D discrete eigenvalue system is $866 \times 360 \times 316$ (about 98 millions). The system is then reduced to 360 subsystems with the matrix size of $866 \times 316 = 273656$ by the reduction method. A total of 11 bound state energies were calculated as shown in Table 4 and graphically displayed in Fig. 4. Note particularly that only the 2D eigenproblems associated with the vertical slices $j = 1, \ldots, 7$ are required for the computation of these bound states whereas other subsystems $j = 8, \ldots, 360$ are not required since all subsystems are independent of each other as Eq. (16) is inferred. In other words, if we are interested in only bound states, we only have to solve seven subsystems for this particular partition. This implies that the computational efforts can be tremendously reduced when compared with a full solution on the original 3D system. Nevertheless, the rest of subsystems were also solved in our experiment and the corresponding energy levels are shown in Fig. 4 as a continuous spectrum out of the confinement potential.

*Subcase* 3.2. $\mu = 90$, 180, or 360 and $\Delta r_c = 0.1$, 0.05, or 0.025 nm. A question on the value of $\mu$, i.e., the partition number in the azimuthal direction is thus evident. To explore the effect of different $\mu$s, we compute the smallest eigenvalue of the subsystem associated with $\theta = 2\pi/\mu$ for a certain $\mu$. This computed eigenvalue approximates the first excited state energy of the model. The ground state energy is not computed in the numerical experiments here since it is embedded in the subsystem with $\theta = 0$ and is thus independent to $\mu$. Table 5 shows the first excited state energies computed by using different partition numbers in the azimuthal direction. As shown in the table, higher partition numbers in the azimuthal direction result in more accurate estimation. The improvement is however not significant. The computed energy levels are accurate up to five significant digits for all three different $\mu$s.

Several remarks on Table 4 and Figs. 5 and 6 are in order. First of all, the global order of the energy levels (denoted by $\lambda_{\text{Global–Ord}}$) depends essentially on the order of the azimuthal index $j$ and the local order

Table 4
Computed discrete energy levels results

| $j$ | $\lambda_{\text{Local-Ord}}$ | $\lambda_{\text{Global-Ord}}$ | $\lambda$ | QN | Time (s) |
|---|---|---|---|---|---|
| 1 | 1 | 1 | 0.1090 | (1, 0, 1) | 2444 |
| 1 | 2 | 4 | 0.1925 | (2, 0, 1) | 539 |
| 1 | 3 | 10 | 0.3136 | (3, 0, 1) | 1855 |
| 2 | 1 | 2 | 0.1393 | (1, 1, 1) | 1757 |
| 2 | 2 | 6 | 0.2477 | (2, 1, 1) | 1116 |
| 3 | 1 | 3 | 0.1767 | (1, 2, 1) | 1183 |
| 3 | 2 | 8 | 0.3025 | (2, 2, 1) | 1463 |
| 4 | 1 | 5 | 0.2181 | (1, 3, 1) | 1126 |
| 5 | 1 | 7 | 0.2615 | (1, 4, 1) | 1506 |
| 6 | 1 | 9 | 0.3055 | (1, 5, 1) | 906 |
| 7 | 1 | 11 | 0.3481 | (1, 6, 1) | 2117 |

The heading indicates the order of the azimuthal index ($j$), the local order of the energy levels in the $j$th subsystem ($\lambda_{\text{Local-Ord}}$), the global order of the energy levels ($\lambda_{\text{Global-Ord}}$), the energy levels $\lambda$, the quantum numbers ($n_r$, $n_\theta$, $n_z$), and the computational time in seconds.

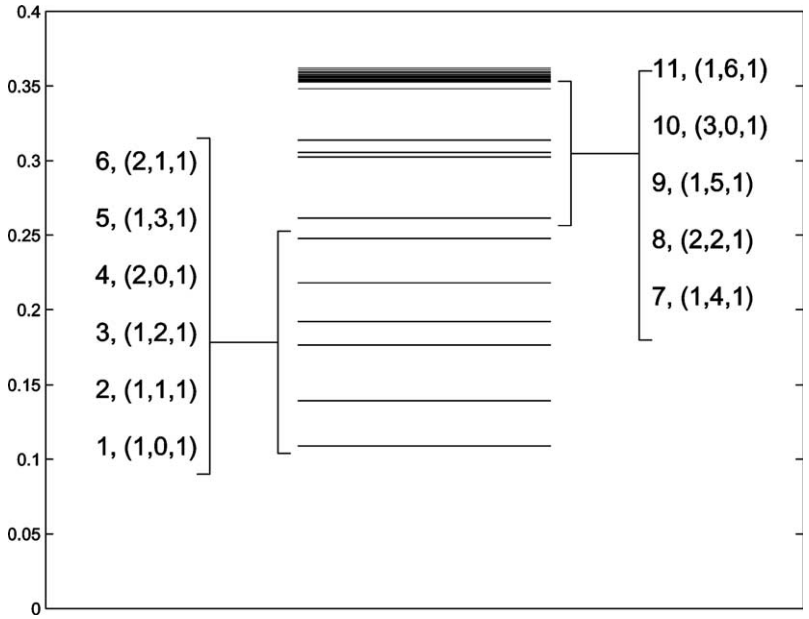


Fig. 4. Spectrum of the energy levels (eigenvalues). The corresponding order and quantum numbers are listed on the two sides of the spectrum.

Table 5
Computational results for the first excited state energy with different mesh lengths ($\Delta r_c$) and different partition number in the azimuthal direction ($\mu$)

| Matrix size | 58,900 | 203,500 | 751,900 |
|---|---|---|---|
| $\Delta r_c$ in nm | 0.1 | 0.05 | 0.025 |
| $\mu = 90$ | 0.13905034 | 0.13921712 | 0.13935382 |
| $\mu = 180$ | 0.13905559 | 0.13922237 | 0.13935907 |
| $\mu = 360$ | 0.13905690 | 0.13922368 | 0.13936038 |

Note that the fine mesh $\Delta r_f = 0.1\Delta r_c$.

of the energy levels is determined by the subsystem (denoted by $\lambda_{\text{Local-Ord}}$ in Table 4). For example, only the first three eigenvalues obtained by solving the first subsystem of Eq. (16) are within the confinement potential. Secondly, the order of the energy levels of a subsystem indicates the number of nodal lines of the corresponding wave function in the radial direction. We use the notation ($n_r$, $n_\theta$, $n_z$) as a quantum number representing the numbers of nodal lines in the radial, azimuthal, and axial directions, respectively. For instance, the second wave function (associated with the first excited state $\lambda_2 = \lambda_{(1,1,1)}$) shown in Fig. 5 has one nodal line in each direction. All the wave functions shown in Figs. 5 and 6 were plotted on the horizontal disk passing through the center of the dot. Thirdly, the computing time required for each eigenvalue is moderate as shown in the last column of Table 4.

We finally note that the small reduced subsystems are closely related to the symmetry of the model problem. Since the wave function is periodic in $\theta$, it can be represented by the truncated Fourier series

$$F(r,\theta,z) = \sum_{l=-\mu/2}^{\mu/2-1} \phi_l(r,z) \mathrm{e}^{\sqrt{-1}l\theta},$$

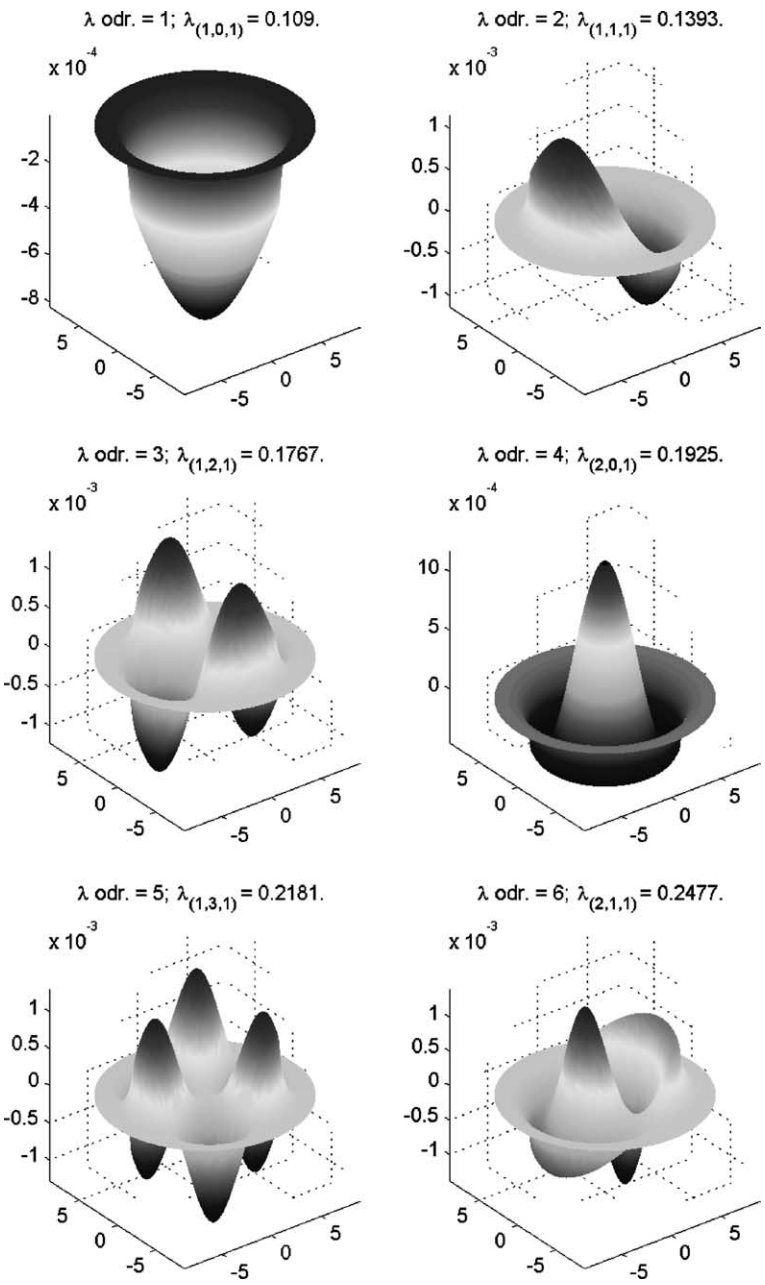


Fig. 5. The wave functions corresponding to the first six smallest energy levels.

where $l$ is the orbital quantum number and $\phi_l$ is the Fourier component in the $(r, z)$ space. Substituting this series in Eq. 1, we obtain a series of 2D problems for which we need to specify different boundary conditions on the line $z = 0$ according to the types (even or odd) of the wave functions $\phi_l$, which is also related to the number of nodal lines $n_\theta = j - 1$ in Table 4. By choosing certain values for $\theta$, the 3D solutions can then be obtained by multiplying the computed 2D solutions with the above exponential function. However,

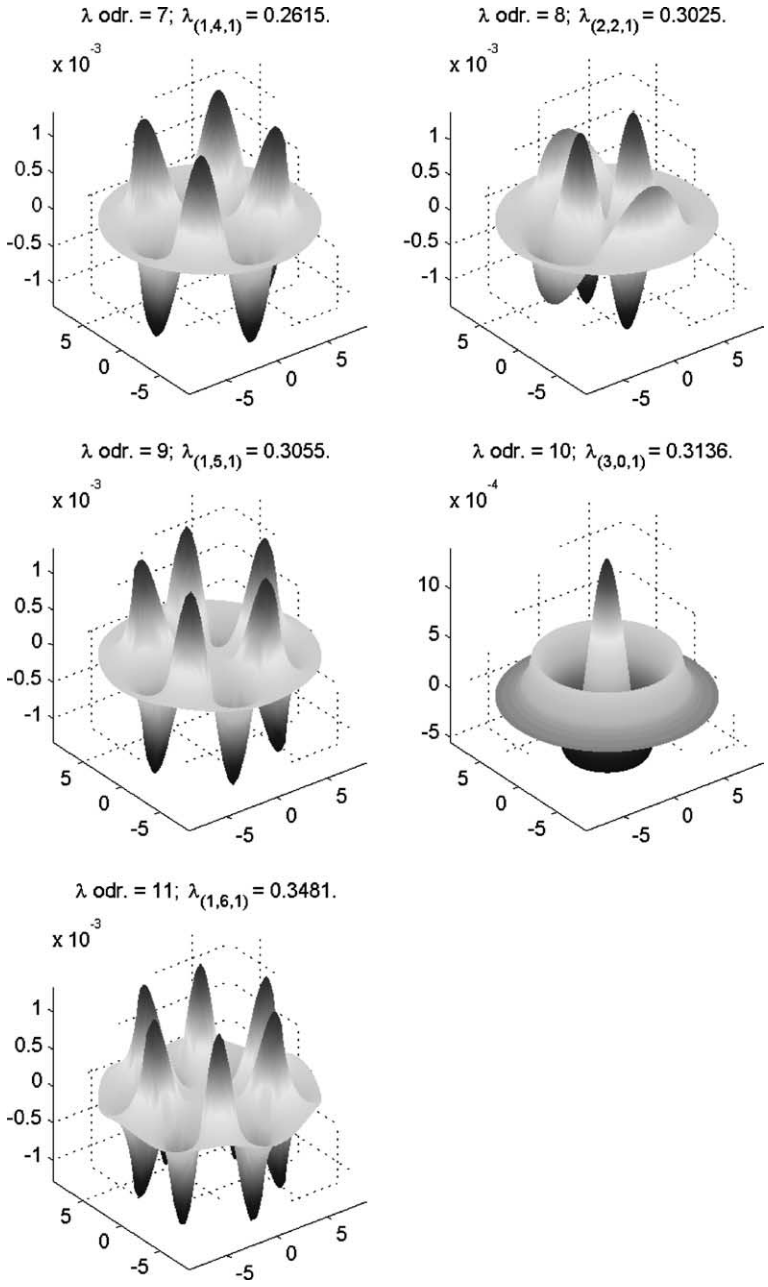


Fig. 6. The wave functions corresponding to the 7th to the 11th smallest energy levels.

when the symmetry is broken as many shapes of the quantum dot being reported in the literature, we inevitably need to deal with 3D discretization. The reduction method proposed here may be extended to more general 3D matrices provided that relatively few rows or columns break the symmetry. This is interesting and challenging topic deserved to be further investigated.

## 6. Conclusion

This paper is concerned with efficient and accurate methods for calculating bound state energies and associated wave functions of semiconductor quantum dots with special interest in the treatment of mathematical difficulties incurred by the nonparabolic band structure. Band nonparabolicity plays an essential role in the study of the effect of spin–orbit splitting in semiconductor heterostructures especially for small size QDs. We present here a discretization scheme and a matrix reduction method that can dramatically reduce huge eigenvalue systems to relatively very small subsystems which are obtained by means of permutations and Fourier matrix transformations. Due to nonparabolicity, these subsystems are of cubic eigenvalue problems for which a nonlinear Jacobi–Davidson method and a deflation scheme are proposed to compute all desired eigenpairs. The order of bound state energies depends essentially on the first few subsystems that in turn are ordered in the azimuthal direction. Moreover, the corresponding wave functions can be characterized by the quantum numbers associated with both of the order of these subsystems and the order of computed eigenvalues of each individual subsystem.

Our methods can be used for various semiconductor materials with various dot sizes. Although the dot is restricted to cylindrical shape in this paper, these methods can be used for other shapes of the dot with some modification on the discretization of the interface condition imposed on the heterojunction. For example, if the interface does not align with the grid points, a weighted finite difference approximation of the interface condition can be used according to the distance between the grid point and the interface. This still preserves the low-rank nature for the deflation scheme. However, we may expect to require more subsystems than that of cylindrical shape since the symmetry is broken. Another example that is of interest is the pyramidal QD. For this type of QD, the domain is not radial symmetric and the reduction scheme can not be applied directly. Different reduction methods should be devised. Finally, the treatment of interface conditions with structured meshes is also a critical issue for QD simulations. We have used here linear finite difference approximation for the interface conditions. The convergence rate can be improved with higher-order approximation. We shall report our numerical results for various shapes of QDs with higher-order approximation of the interface conditions in future papers.

## Acknowledgements

The authors are grateful to the anonymous referees for carefully reading the manuscript and the helpful comments. This work is partially supported by the National Science Council and the National Center for Theoretical Sciences in Taiwan.

## References

[1] L. Jacak, P. Hawrylak, A. Wójs, Quantum Dots, Springer, Berlin, 1998.
[2] R. Heitz, M. Veit, N.N. Ledentsov, A. Hoffmann, D. Bimberg, V.M. Ustinov, P.S. Kopév, Z.I. Alferov, Energy relaxation by multiphonon processes in InAs/GaAs quantum dots, Phys. Rev. B 56 (1997) 10435–10445.
[3] G. Medeiros-Ribeiro, J.M. Garcia, P.M. Petroff, Charging dynamics of InAs self-assembled quantum dots, Phys. Rev. B 56 (1997) 3609–3612.
[4] S. Maimon, E. Finkman, G. Bahir, S.E. Schacham, J.M. Garcia, P.M. Petroff, Intersublevel transitions in InAs/GaAs quantum dots infrared photodetectors, Appl. Phys. Lett. 73 (1998) 2003–2005.
[5] L. Harris, D.J. Mowbray, M.S. Skolnick, M. Hopkinson, G. Hill, Emission spectra and mode structure of InAs/GaAs self-organized quantum dot lasers, Appl. Phys. Lett. 73 (1998) 969–971.
[6] G. Iannaccone, A. Trellakis, U. Ravaioli, Simulation of a quantum-dot flash memory, J. Appl. Phys. 84 (9) (1998) 5032–5036.
[7] G. Burkard, D. Loss, D.P. DiVincenzo, Couple quantum dots as quantum gates, Phys. Rev. B 59 (1999) 2070–2078.
[8] J.W. Gray, D. Childs, S. Malik, P. Siverns, C. Roberts, P.N. Stavrinou, M. Whitehead, R. Murray, G. Parry, Quantum dot resonant cavitylight emitting diode operating near 1300 nm, Electron. Lett. 35 (1999) 242.

[9] A.J. Williamson, A. Zunger, InAs quantum dots: predicted electronic structure of free-standing versus GaAs-embedded structures, Phys. Rev. B 59 (1999) 15819–15824.
[10] F.M. Peeters, V.A. Schweigert, Two-electron quantum disks, Phys. Rev. B 53 (1996) 1468–1474.
[11] J. Shumway, L.R.C. Fonseca, J.P. Leburton, R.M. Martin, D.M. Ceperley, Electronic structure of self-assembled quantum dots: comparison between density functional theory and diffusion quantum monte carlo, Physica E 8 (2000) 260–268.
[12] P. Harrison, Quantum Wells, Wires, and Dots: Theoretical and Computational Physics, Wiley, New York, 2000.
[13] E.A. de Andrada e Silva, G.C.L. Rocca, F. Bassani, Spin–orbit splitting of electronic states in semiconductor asymmetric quantum wells, Phys. Rev. B 55 (24) (1997) 16293.
[14] E.A. de Andrada e Silva, Optical transition energies for lead-salt semiconductor quantum wells, Phys. Rev. B 60 (12) (1999) 8859.
[15] Th. Schapers, G. Engels, J. Lange, Th. Klocke, M. Hollfelder, H. Luth, Effect of the heterointerface on the spin splitting in modulation doped $In_{(x)}Ga_{(1-x)}As/InP$ quantum wells for $b \to 0$, J. Appl. Phys. 83 (8) (1998) 4324.
[16] O. Voskoboynikov, C.P. Lee, O. Tretyak, Spin–orbit splitting in semiconductor quantum dots with a parabolic confinement potential, Phys. Rev. B 63 (2001) 165306.
[17] G.A. Prinz, Magnetoelectronics, Science 282 (1998) 1660–1663.
[18] B.E. Kane, A silicon-based nuclear spin quantum computer, Nature 393 (1998) 133.
[19] J. Fabian, S.D. Sarma, Spin relaxation of conduction electrons, J. Vac. Sci. Technol. B 17 (1708).
[20] S. Bandyopadhyay, Self-assembled nanoelectronic quantum computer based on the Rashba effect in quantum dots, Phys. Rev. B 61 (20) (2000) 13813.
[21] M.-C. Lai, A note on finite difference discretizations for Poisson equation on a disk, Numer. Methods Partial Differ. Equ. 17 (3) (2001) 199–203.
[22] T.-M. Hwang, W. Wang, Analyzing and visualizing a discretized semilinear elliptic problem with Neumann boundary conditions, Numer. Methods Partial Differ. Equ. 18 (3) (2002) 261–279.
[23] Z. Bai, G. Sleijpen, H. van der Vorst, Nonlinear eigenvalue problems, in: Z. Bai, J. Demmel, J. Dongarra, A. Ruhe, H. van der Vorst (Eds.), Templates for the Solution of Algebraic Eigenvalue Problems: A Practical Guide, SIAM, Philadelphia, 2000 (Chapter 9).
[24] Z. Bai, J. Demmel, J. Dongarra, A. Ruhe, H. van der Vorst, Templates for the Solution of Algebraic Eigenvalue Problems: A Practical Guide, SIAM, Philadelphia, 2000.
[25] K. Meerbergen, Locking and restarting quadratic eigenvalue solvers, SIAM J. Sci. Comput. 22 (5) (2001) 1814–1839.
[26] J.-S. Guo, W.-W. Lin, C.-S. Wang, Nonequivalence deflation for the solution of matrix latent value problems, Linear Algebra Appl. 231 (1995) 15–45.
[27] J. Stoer, R. Bulirsch, Introduction to Numerical Analysis, Springer, Berlin, 2002.
[28] W.V. Schoenfeld, Spectroscopy of the electronic structure of coupled quantum dots systems, Ph.D. Thesis, Materials Department, University of California, Santa Barbara, July 2000.
[29] Y. Li, J.-L. Liu, O. Voskoboynikov, C.P. Lee, S.M. Sze, Electron energy level calculations for cylindrical narrow gap semiconductor quantum dot, Comput. Phys. Commun. 140 (2001) 399–404.